Preprint Title	Realizing and Adjusting the Thermoelectric Application of MoO$_3$ Monolayer via Oxygen Vacancies
Authors	Wenwen Zheng, Wei Cao, Ziyu Wang, Huixiong Deng, Jing Shi and Rui Xiong
Publication Date	23 Jul 2019
Article Type	Full Research Paper
ORCID® iDs	Ziyu Wang - https://orcid.org/0000-0001-9718-1263

Realizing and Adjusting the Thermoelectric Application of MoO₃ Monolayer via Oxygen Vacancies

Wenwen Zheng[1], Wei Cao[2], Ziyu Wang[3,*], Huixiong Deng[4], Jing Shi[2] and Rui Xiong[2,†]

1. *Hubei Key Laboratory of Optical Information and Pattern Recognition, School of Mathematics and Physics, Wuhan Institute of Technology, Wuhan 430205, PR China.*

2. *Key Laboratory of Artifcial Micro- and Nano-Structures of Ministry of Education, School of Physics and Technology, Wuhan University, Wuhan 430072, PR China.*

3. *The Institute of Technological Sciences, Wuhan University, Wuhan 430072, PR China.*

4. *State Key Laboratory of Superlattices and Microstructures, Institute of Semiconductors, Chinese Academy of Sciences, P. O. Box 912, Beijing 100083, PR China.*

Abstract

We have investigated the thermoelectric properties of pristine MoO₃ monolayer and its defective structures with different oxygen vacancies by using first-principles method combined with Boltzmann transport theory. Our results show that the thermoelectric properties of MoO₃ monolayer exhibit an

* zywang@whu.edu.cn

† xiongrui@whu.edu.cn

evident anisotropic behavior which is caused by the similar anisotropic phenomenon of electronic conductivity and thermal conductivity. The ZT values along x-axis and y-axis directions are 0.72 and 0.08 at 300K, respectively. Moreover, the creation of oxygen vacancies proves to be an effective way to enhance the ZT values of MoO₃ monolayer which is caused by the sharp peak near the Fermi level in density of states. The increased ZT values can reach 0.84 (x-axis) and 0.12 (y-axis) at 300K.

Keywords: molybdenum trioxides, thermoelectric, oxygen vacancy

1. Introduction

Thermoelectric materials which can directly convert temperature gradient to voltage gradient and *vice versa* provide a valid strategy for global energy crisis. Owing to its unique ability of utilizing waste heat without generating any greenhouse gas, thermoelectric technology has attracted increasing attention.[1] Nevertheless, the application of thermoelectric materials is limited by its low energy conversion efficiency. The performance of thermoelectric materials is usually measured by a figures of merit (ZT) defined as $ZT = S^2\sigma T / \kappa$, where S, σ, T, and κ represent Seebeck coefficient, electronic conductivity, temperature, and thermal conductivity, respectively.[2,3] In the past decade, great efforts have been made to boost the capability of thermoelectric materials.[4] Unfortunately, the application of conventional thermoelectric materials is still limited on account of inefficiency, high-cost, stability and toxicity problems.

As a promising candidate to address these severe challenges, transition metal oxides (TMOs) contain a vast family of low-cost and environmentally friendly materials. From insulating to

semiconducting and conducting, TMOs exhibit wide-ranging electronic and magnetic characteristics which depend on their geometric structure, doping concentration and stoichiometry ratio.[5] TMOs have been used in many fields as Li-ion battery, electrochemical capacitors and fuel cells.[6] Meanwhile, the thermoelectric application of TMOs-based materials has been explored and their poor efficiency is still the major difficulty.[7]

Among these TMOs, layered molybdenum trioxide (MoO_3) has attracted extensive attention as a potential electrode material in electrochemical products[8] and Li-ion battery[9-12]. Like most TMOs, bulk MoO_3 owns a wide band gap (about 3.0 eV) and low electronic conductivity, which seems inappropriate for thermoelectric devices. However, the electronic properties (including band gap and conductivity) of MoO_3 are strongly dependent on oxygen vacancy concentrations. Many ionic intercalation approaches as hydrogen-ion[13] and solar-light irradiation[14] can turn MoO_3 into MoO_{3-x} and hence raise its electronic conductivity. Understanding the effect of oxygen vacancies in MoO_3 is very beneficial to its thermoelectric applications. Besides, the low-dimensional materials exhibit better thermoelectric performance than bulk materials.[15] In view of its layered structure, few-layer MoO_3 nanosheets have been synthesized already in experiment like graphene.[13,14,16,17] Theoretical research has proved that few-layer MoO_3 possesses a markedly high carrier mobility above 3000 $cm^2V^{-1}s^{-1}$.[18] Therefore, it is of profound significance to explore the thermoelectric properties of MoO_3 monolayer and discuss the effect of oxygen vacancies on it.

2. Method

In this work, we evaluate the thermoelectric properties of MoO_3 monolayer by the Boltzmann transport theory and first-principles calculations. The calculations on electronic properties of MoO_3 monolayer are performed by density functional theory (DFT) as implemented in Vienna Ab Inito Simulation Package (VASP) code [19,20]. We utilize the generalized gradient approximation (GGA) of Perdew-Burke-Ernzerhof (PBE)[21] pseudopotentials without the spin-orbit interaction. Since PBE functional fails to capture the electronic and optical properties of bulk MoO_3 by a large margin (band gap less than half of experimental measurement), we also employ Heyd–Scuseria–Ernzerhof (HSE06) hybrid functional potential [22,23] to obtain a more accurate band sturcture. The vacuum distance is set to 15 Å to avoid the interactions between the MoO_3 monolayer and its periodic images. A plane-wave basis set with a cutoff of 520 eV and the k-mesh is tested to be 10×10×1 for the purpose of convergence.

Based on the results of the electronic structure, the electronic transport properties can be obtained by the Boltzmann transport theory and constant scattering time approximation as implemented in the BoltzTraP code[24]. To get reliable electronic transport coefficients, a denser k-point mesh as 40×40×1 is used to obtain converged results. Based on the framework of Boltzmann transport theory, the electrical conductivity σ and the Seebeck coefficient S can be expressed as:

$$\sigma = e^2 \int d\varepsilon \left(-\frac{\partial f_0}{\partial \varepsilon} \right) \Sigma(\varepsilon) , (1)$$

$$S = \frac{ek_B}{\sigma} \int d\varepsilon \left(-\frac{\partial f_0}{\partial \varepsilon} \right) \Sigma(\varepsilon) \frac{\varepsilon - u}{k_B T} \text{ , (2)}$$

$$\left(-\frac{\partial f_0}{\partial \varepsilon} \right) = \frac{1}{k_B T} \frac{e^{\left(\frac{\varepsilon - u}{k_B T} \right)}}{(e^{\left(\frac{\varepsilon - u}{k_B T} \right)} + 1)^2} \text{ , (3)}$$

where the u is the chemical potential (corresponds to the carrier concentration), k_B is the Boltzmann constant, e is the electron charge and T is the he absolute temperature. $\Sigma(\varepsilon)$ is the so-called transport distribution function [25]:

$$\Sigma(\varepsilon) = \sum_{\vec{k}} v(\vec{k})^2 \tau(\vec{k}) \delta(\varepsilon - \varepsilon(\vec{k})) \text{ , (4)}$$

where $v(\vec{k})$ is the group velocity of the carriers and $\tau(\vec{k})$ is the relaxation time, respectively. The electronic thermal conductivity κ_e is obtained by the Wiedemann-Franz law: $\kappa_e = L\sigma T$, where L is the Lorenz number. For the calculation of the relaxation time τ, we apply the deformation potential theory [26] where τ is estimated by $\tau = \mu m^* / e$ and the carrier mobility μ is given by

$\mu = \frac{e\hbar^3 C_{2D}}{k_B T m^* m_d E_1^2}$. All the corresponding parameters of carrier mobility and effective mass are taken from ref. 18 as summarized in Tab. 1.

As for phononic transport properties, we calculate the lattice thermal conductivity by the Boltzmann transport theory as implemented in the Quantum ESPRESSO (QE) package[27,28] and ShengBTE code[29]. The pseudopotential files are obtained from the Standard Solid-State Pseudopotentials library[30] and kinetic energy cutoff is set to be 80 Ry. The density functional

perturbation theory (DFPT) is adopted for the calculation of second-order (harmonic) interatomic force constants (IFCs) from the QE package[27] and third-order (anharmonic) IFCs are obtained from ShengBTE code[29] with the maximum atomic interaction distance of the sixth neighbor in the 4×4×1 supercell. Here, a dense phonon q-grid of 52×52×1 is used to compute the lattice thermal conductivity of MoO_3 and the scale parameter for smearing is set to 0.1.

3. Results and discussion

As shown in Fig. 1(a), the MoO_3 monolayer is cut from orthorhombic α-MoO_3 bulk structure (space group *Pbnm*) and the primitive cell contains 8 atoms. Apparently, there are three distinguishable oxygen atoms which are connected to different molybdenum atoms and they are labeled by different colors. The relaxed lattice constants of MoO_3 monolayer are a=3.68 Å and b=3.93 Å, which are similar to the bulk experimental data of 3.70 and 3.96 Å[31]. In Fig. 1(b), we give the electronic band structure of the MoO_3 monolayer PBE potential and HSE06 hybrid functional potential. One can see clearly that both the two different potentials exhibit similar electronic band structures for the larger energy gaps. The minimum point of the first conduction band (CBM) appears at the Γ point, while the maximum of the first valence band (VBM) appears at a point along the S point. The indirect bandgap of MoO_3 monolayer is 1.79 eV for PBE and 2.85 eV for HSE06 which is consistent with previous studies[18,32]. Since MoO_3 monolayer is a wide-gap semiconductor, it is likely to exhibit a giant Seebeck coefficient and low electronic conductivity. The discrepancies between PBE potential and HSE06 hybrid functional are inconspicuous when computing the Seebeck

coefficient and electronic conductivity. Considering the extremely slow speed of HSE06 hybrid functional potential, we use PBE potential to get the electronic transport properties of MoO_3 monolayer in the following work.

As for the phononic properties, the phonon dispersion in the high-symmetry directions of the first Brillouin zone for MoO_3 monolayer is plotted in Figs. 1(c). There is no imaginary frequency which ensures the stability of MoO_3 monolayer. It is well known that the acoustical phonon branches possess large group velocities and the mainly decide lattice thermal conductivity.[33] As the dashed lines pointed out in Figs. 1(c), the acoustic phonon group velocity along Γ-Y direction is larger than that along Γ-X direction, which is an indication of anisotropic phonon transport. The lattice thermal conductivity κ_{ph} along different directions as a function of temperature is depicted in Fig. 1(d). It is obvious that the thermal transport property of MoO_3 monolayer presents an anisotropic behavior, where the lattice thermal conductivity along the x-axis direction is higher than that along the y-axis direction. At room temperature, κ_{ph} is 5.38 W/mK and 3.07 W/mK along the x-axis and y-axis direction, respectively. As a result of the intrinsic enhancement in phonon-phonon scattering with temperature, the lattice thermal conductivity of MoO_3 monolayer decreases gradually with temperature increasing which follows a $1/T$ dependence like most crystalline materials.

In Figs. 2(a)-2(c), we demonstrate the electronic transport properties of MoO_3 monolayer as a function of carrier concentration at three typical temperatures (T =300, 500, and 700 K). It should be noted that the n-type and p-type transport properties of MoO_3 monolayer are uniform. Therefore, only

p-type cases are exhibited here. In Fig. 2(a), the Seebeck coefficient S of MoO$_3$ monolayer along the x-axis and y-axis directions possesses the same value. With temperature increasing from 300 K to 700 K, the Seebeck coefficient of MoO$_3$ monolayer decreases gradually which coincides with the relation: $S \propto (1/n)^{2/3}$.[3] The maximum value of S for MoO$_3$ monolayer can achieve 1.69 mV/K at room temperature. Such huge S value can be explained by the proportional relationship between Seebeck coefficient and bandgap.[34] Unlike the phenomenon of Seebeck coefficient, the electronic conductivity and electronic thermal conductivity exhibit a clear anisotropic behavior which is contributed to the anisotropic relaxation time.[18] Fig. 2(b) reveals that the electronic conductivity along the x-axis direction is obviously much higher than that along the y-axis direction. For example, we have σ =8268 S/m along x-axis direction, while σ =338 S/m along y-axis direction at room temperature and n =10^{13} cm^{-2}. The electronic thermal conductivity of MoO$_3$ monolayer equally exhibits an evident anisotropic behavior and boots gradually as temperature increases in Fig. 2(c). Particularly, κ_e = 1.29 W/mK and 0.032 W/mK for x-axis and y-axis at room temperature and n =10^{13} cm^{-2}. By combining the phononic and electronic transport properties presented above, we can obtain the ZT value of MoO$_3$ monolayer as a function of carrier concentration in Fig. 2(d). It is found that the ZT value along x-axis direction is much higher than that along y-axis direction. The maximum ZT value along x-axis can reach 0.84 at 700K which is nearly four times than the value along y-axis. The carrier concentration needed to attain the maximum ZT value in the n-type MoO$_3$ monolayer is about 1.16×10^{13} cm^{-2} (x-axis) and 6.67×10^{13} cm^{-2} (y-axis).

In order to strengthen the thermoelectric performance of MoO$_3$ monolayer, we decided to introduce oxygen vacancies in it. We remove one oxygen atom in the 3×3×1 supercell (72 atoms) to construct charge neutral defect and the stoichiometric proportion is MoO$_{2.94}$. Since there are three types of oxygen atoms in the primitive cell, we named the three defective structures by V$_{O1}$, V$_{O2}$ and V$_{O3}$. The formation energy E_f of a charge neutral defect is defined as: $E_f = E_{tot}(\text{defect}) - E_{tot}(\text{supercll}) + \frac{1}{2}E_{tot}(O_2)$, where $E_{tot}(\text{defect})$ is total energy of the supercell containing the defect, $E_{tot}(\text{supercll})$ is total energy of the perfect supercell and $E_{tot}(O_2)$ is the total energy of the oxygen molecules. Then we calculate the formation energies and band gaps of these defect structures. The absolute values of formation energy are 2.074 eV (V$_{O1}$), 2.076 eV (V$_{O2}$) and 4.108 eV (V$_{O3}$) while the band gaps are 0.837 eV (V$_{O1}$), 0.797 eV (V$_{O2}$) and 0.831 eV (V$_{O3}$). Different from the results of bulk MoO3, the three defected structures finally lead to only two stable sturctures after relaxation which is contributed the absence of interlayer van der Waals forces.

It is a hard work to calculate the lattice thermal conductivity and electronic relaxation time of 71 atoms primitive cell by Boltzmann transport theory. So, we assume that the lattice thermal conductivity and electronic relaxation time remains unchanged. In fact, these oxygen vacancies can result in the reduction of the lattice thermal conductivity due to phonon scattering at the vacancies and the final ZT values will be higher. For briefness and clarity, we just display the maximum ZT values in Fig. 3. It can be noted clearly that when vacancies are induced, the ZT values along x-axis increase immediately, especially around low temperature region. However, the cases along y-axis are distinguishing. In Fig. 3(b), the ZT values of V$_{O3}$ along y-axis are obviously higher than

other cases at usual working temperature 300K~600K. The conclusion is that generating the V_{O3} will be the best way to enhance thermoelectric properties of MoO$_3$ monolayer. The maximum ZT values along x-axis and y-axis are 0.83 and 0.12 at room temperature which indicates that defective MoO$_3$ monolayer is indeed a promising candidate for good thermoelectric materials.

To make clear reason of the strengthening in the thermoelectric properties, we give the electronic density of states (DOS) of these structures in Fig. 4. With the import of oxygen vacancies, the Fermi level has moved closer to the conduction band and an asymmetric sharp peak occurs around the bottom of the conduction band as pointed out in Fig. 4(a). The sharp peak in DOS mainly comes from the Mo atom through the projected DOS for Mo and O atoms presented in Fig. 4(b) and (c). Additionally, the values for V_{O1} and V_{O2} are almost the same which means they lead to the same structure. The structural dependency of defective MoO$_3$ monolayer can be reflected by the insets of Fig. 4(b) and (c). Previous theoretical research shows that a narrow and sharp peaks in the electronic density of states around Fermi level will generate a great transport distribution function and maximize the power factor $S^2\sigma$.[25,35] Especially for V_{O3}, the sharp peak is more clear than other structures which makes for the best thermoelectric performance among them. Oxygen vacancies can act as shallow donors and destroy the crystal symmetry, thereby enlarging the carrier concentration.

4. Conclusions

In summary, we have presented a comprehensive study of the thermoelectric properties of MoO$_3$ monolayer by first-principles calculations and Boltzmann theory. Results indicate that MoO$_3$

monolayer exhibit better thermoelectric performance along x-axis than that along y-axis because of the strong anisotropic behavior of electronic conductivity and thermal conductivity. The ZT value along x-axis can reach 0.72 at 300K which is much higher than other oxides. On the other hand, we find that the introduction of oxygen vacancy is an efficient way to improve the thermoelectric performance of MoO_3 monolayer. Such improvement can be attributed to a sharp peak in electronic density of states which leads to a large transport distribution function. The structure with O3 vacancies possesses a maximum room temperature ZT value of 0.84 (x-axis) and 0.12 (y-axis). Our work provides helpful theoretical guidance on the thermoelectric applications of two-dimensional TMOs.

Acknowledgements

References

[1] M. Zebarjadi, K. Esfarjani, M. S. Dresselhaus, Z. F. Ren, and G. Chen, Energy & Environmental Science **5** (1), 5147 (2012).

[2] Lon E. Bell, Science **321** (5895), 1457 (2008).

[3] G. Jeffrey Snyder and Eric S. Toberer, Nature Materials **7**, 105 (2008).

[4] Xiao Zhang and Li-Dong Zhao, Journal of Materiomics **1** (2), 92 (2015).

[5] Warren E. Pickett, Reviews of Modern Physics **61** (2), 433 (1989).

[6] Changzhou Yuan, Hao Bin Wu, Yi Xie, and Xiong Wen Lou, Angewandte Chemie International Edition **53** (6), 1488 (2014).

[7] Sumeet Walia, Sivacarendran Balendhran, Hussein Nili, Serge Zhuiykov, Gary Rosengarten, Qing Hua Wang, Madhu Bhaskaran, Sharath Sriram, Michael S. Strano, and Kourosh Kalantar-zadeh, Progress in Materials Science **58** (8), 1443 (2013).

[8] Torsten Brezesinski, John Wang, Sarah H. Tolbert, and Bruce Dunn, Nature Materials **9**, 146 (2010).

9   L. Q Mai, B. Hu, W. Chen, Y. Y Qi, C. S Lao, R. S Yang, Y. Dai, and Z. L Wang, Advanced Materials **19** (21), 3712 (2007).

10   Jun Song Chen, Yan Ling Cheah, Srinivasan Madhavi, and Xiong Wen Lou, The Journal of Physical Chemistry C **114** (18), 8675 (2010).

11   Zhiyu Wang, Srinivasan Madhavi, and Xiong Wen Lou, The Journal of Physical Chemistry C **116** (23), 12508 (2012).

12   Tianqi Li, Majid Beidaghi, Xu Xiao, Liang Huang, Zhimi Hu, Wanmei Sun, Xun Chen, Yury Gogotsi, and Jun Zhou, Nano Energy **26**, 100 (2016).

13   Sivacarendran Balendhran, Junkai Deng, Jian Zhen Ou, Sumeet Walia, James Scott, Jianshi Tang, Kang L. Wang, Matthew R. Field, Salvy Russo, Serge Zhuiykov, Michael S. Strano, Nikhil Medhekar, Sharath Sriram, Madhu Bhaskaran, and Kourosh Kalantar-zadeh, Advanced Materials **25** (1), 109 (2013).

14   Manal M. Y. A. Alsaif, Adam F. Chrimes, Torben Daeneke, Sivacarendran Balendhran, Darin O. Bellisario, Youngwoo Son, Matthew R. Field, Wei Zhang, Hussein Nili, Emily P. Nguyen, Kay Latham, Joel van Embden, Michael S. Strano, Jian Zhen Ou, and Kourosh Kalantar-zadeh, Advanced Functional Materials **26** (1), 91 (2016).

15   M. S Dresselhaus, G. Chen, M. Y Tang, R. G Yang, H. Lee, D. Z Wang, Z. F Ren, J. P. Fleurial, and P. Gogna, Advanced Materials **19** (8), 1043 (2007).

16   Sivacarendran Balendhran, Sumeet Walia, Manal Alsaif, Emily P. Nguyen, Jian Zhen Ou, Serge Zhuiykov, Sharath Sriram, Madhu Bhaskaran, and Kourosh Kalantar-zadeh, ACS Nano **7** (11), 9753 (2013).

17   Kourosh Kalantar-zadeh, Jianshi Tang, Minsheng Wang, Kang L. Wang, Alexandros Shailos, Kosmas Galatsis, Robert Kojima, Veronica Strong, Andrew Lech, Wojtek Wlodarski, and Richard B. Kaner, Nanoscale **2** (3), 429 (2010).

18   Wei-Bing Zhang, Qian Qu, and Kang Lai, ACS Applied Materials & Interfaces **9** (2), 1702 (2017).

19   G. Kresse and J. Furthmüller, Physical Review B **54** (16), 11169 (1996).

20   G. Kresse and J. Furthmüller, Computational Materials Science **6** (1), 15 (1996).

21   John P. Perdew, Kieron Burke, and Matthias Ernzerhof, Physical Review Letters **77** (18), 3865 (1996).

22   Jochen Heyd, Gustavo E. Scuseria, and Matthias Ernzerhof, The Journal of Chemical Physics **118** (18), 8207 (2003).

23   Aliaksandr V. Krukau, Oleg A. Vydrov, Artur F. Izmaylov, and Gustavo E. Scuseria, The Journal of Chemical Physics **125** (22), 224106 (2006).

24   Georg K. H. Madsen and David J. Singh, Computer Physics Communications **175** (1), 67 (2006).

25   G. D. Mahan and J. O. Sofo, Proceedings of the National Academy of Sciences **93** (15), 7436 (1996).

26   J. Bardeen and W. Shockley, Physical Review **80** (1), 72 (1950).

27   P. Giannozzi, J. Phys.: Condens. Matter **21**, 395502 (2009).

28   Paolo Giannozzi, Oliviero Andreussi, Thomas Brumme, Oana Bunau, M. Buongiorno Nardelli, Matteo Calandra, Roberto Car, Carlo Cavazzoni, Davide Ceresoli, and Matteo Cococcioni,   Journal of Physics: Condensed Matter **29** (46), 465901 (2017).

29   Wu Li, Jesús Carrete, Nebil A. Katcho, and Natalio Mingo,   Computer Physics Communications **185** (6), 1747 (2014).

30   Gianluca Prandini, Antimo Marrazzo, Ivano E. Castelli, Nicolas Mounet, and Nicola Marzari,   npj Computational Materials **4** (1), 72 (2018).

31   Husin Sitepu,   Powder Diffraction **24** (4), 315 (2009).

32   Fengyu Li and Zhongfang Chen,   Nanoscale **5** (12), 5321 (2013).

33   Paothep Pichanusakorn and Prabhakar Bandaru,   Materials Science and Engineering: R: Reports **67** (2), 19 (2010).

34   Nguyen T. Hung, Ahmad R. T. Nugraha, Eddwi H. Hasdeo, Mildred S. Dresselhaus, and Riichiro Saito,   Physical Review B **92** (16), 165426 (2015).

35   Sit Kerdsongpanya, Björn Alling, and Per Eklund,   Physical Review B **86** (19), 195140 (2012).

Figures & Tables

Table 1. The effective mass (m^*), carrier mobility (μ) and relaxation time (τ) along the x and y

directions of MoO_3 monolayer at 300 K.

Carriers	m_x^*/m_0	m_y^*/m_0	μ_x (cm^{2}V^{-1}s^{-1})	μ_y (cm^{2}V^{-1}s^{-1})	τ_x (ps)	τ_y (ps)
PBE						
Electron	0.873	0.594	1608.81	37.52	0.786	0.012
Hole	2.064	0.974	800.57	25.56	0.925	0.013
HSE06						
Electron	1.056	0.588	793.59	33.60	0.469	0.011
Hole	1.669	0.910	396.35	19.99	0.370	0.010
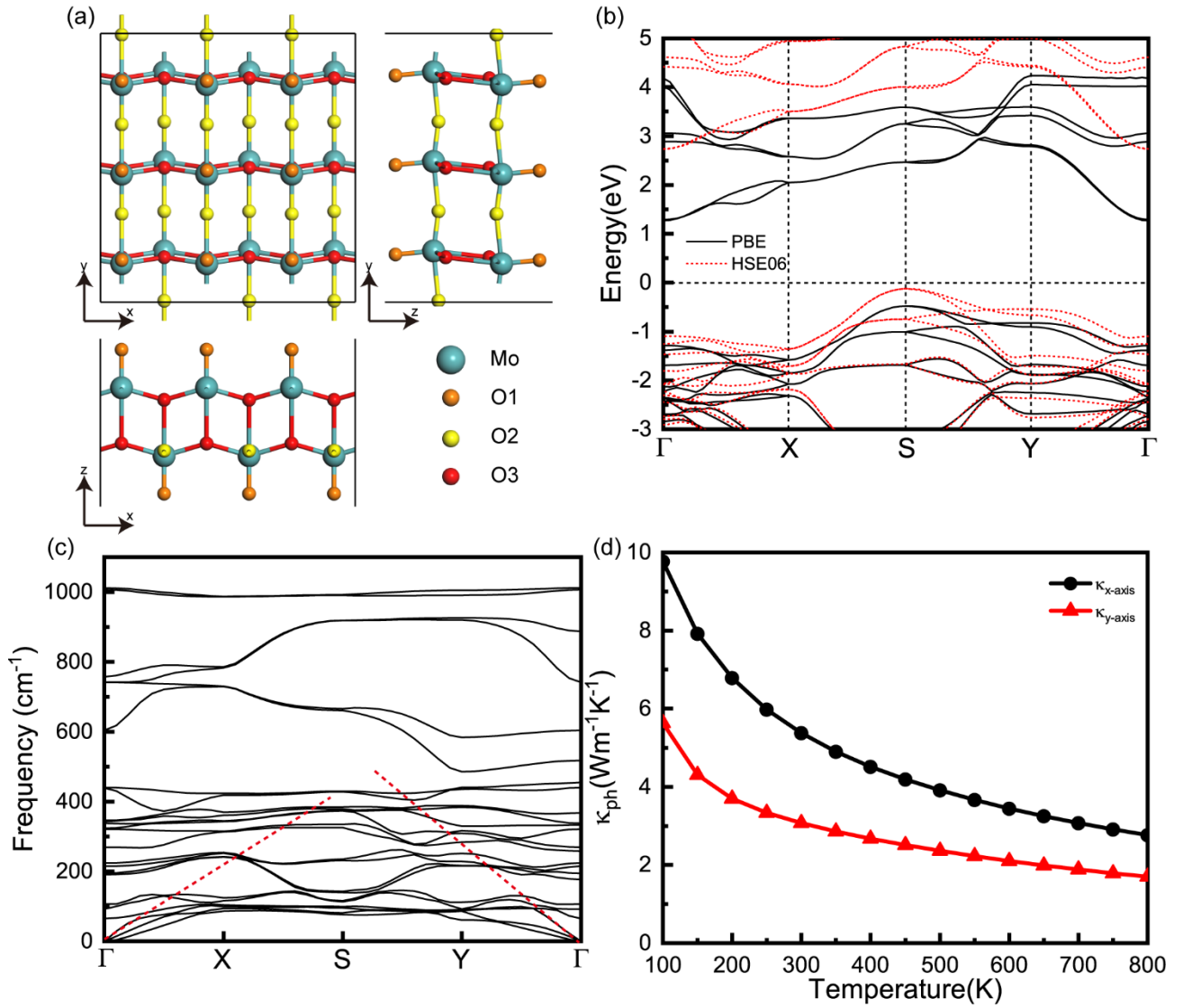
Figure 1. (a) Crystal structures of MoO_3 monolayer (3×3×1 supercell): top and side views. (b) The electronic band structure and (c) phonon dispersion of MoO_3 monolayer along the high-symmetry path. (d) The lattice thermal conductivity κ_{ph} of MoO_3 monolayer along different directions as a function of temperature.
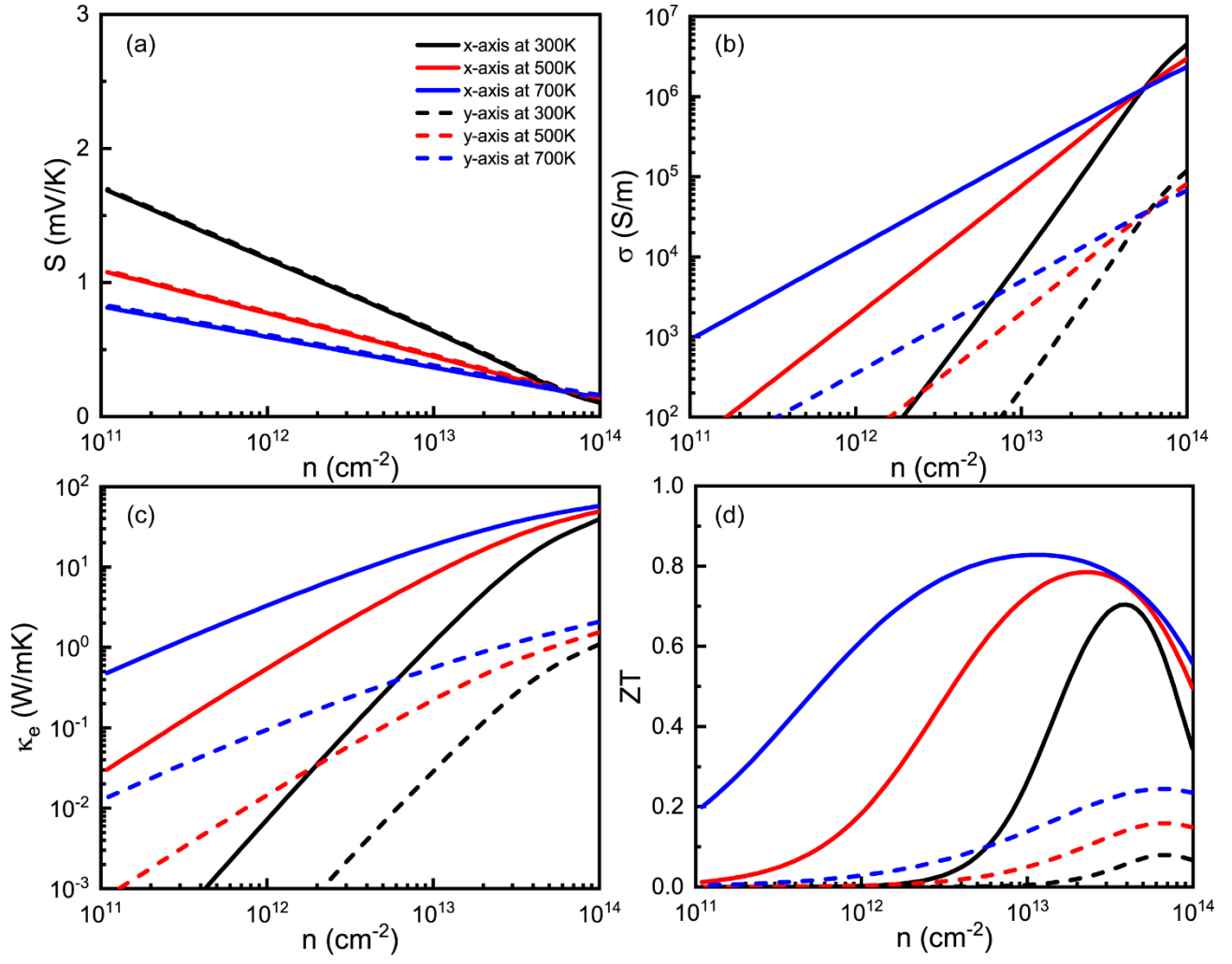
Figure 2. Transport and thermoelectric properties of MoO$_3$ monolayer. (a) Seebeck coefficient S, (b) electronic conductivity σ, (c) electronic thermal conductivity κ_e and (d) ZT values as a function of the carrier concentration.
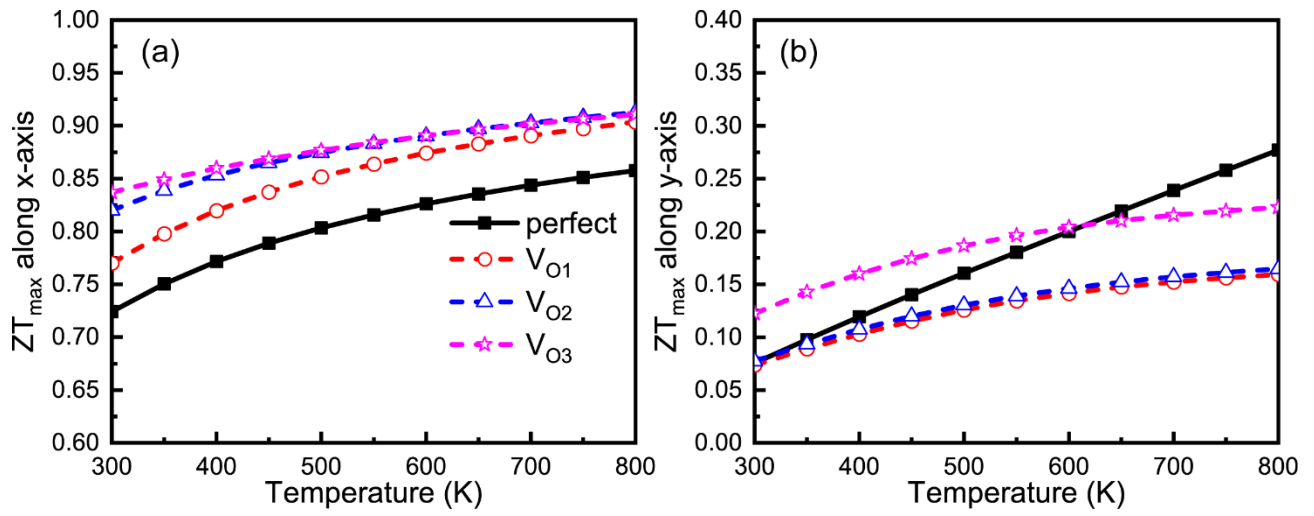
Figure 3. The maximum ZT values as a function of temperatures along (a) x-axis and (b) y-axis.
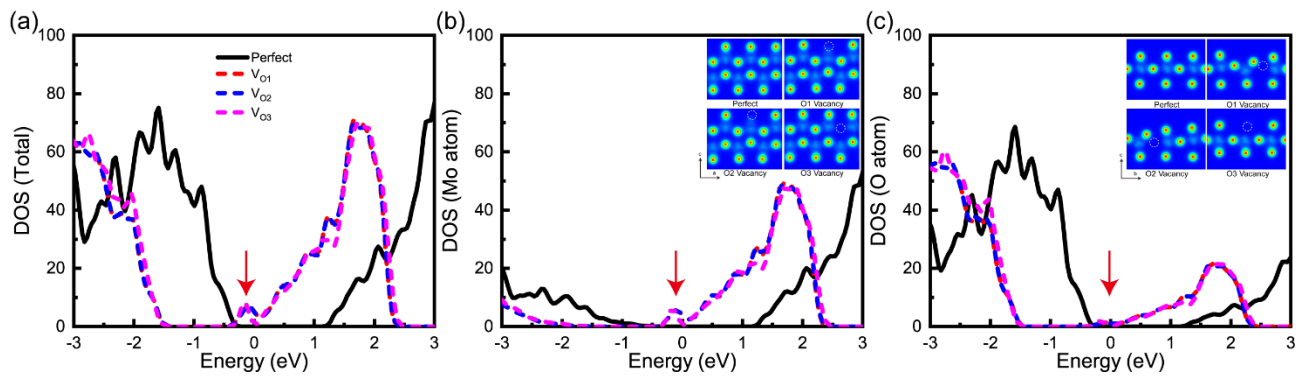
Figure 4. Calculated (a) total electronic density of states (DOS) and projected DOS for (b) Mo and (c) O atoms of MoO$_3$ monolayer. The insets of (b) and (c) denote the total charge density from different views.